Ultra-Fast Tunable Optoelectronic Full-Adder Based on Photonic Crystal Ring Resonators Covered By Graphene Nanoshells

Saleh Naghizade
Islamic Azad University Tabriz Branch
Hamed Saghaei (h.saghaei@iaushk.ac.ir)
Islamic Azad University Shahrekord Branch https://orcid.org/0000-0001-5588-3726

Research Article

Keywords: Full-adder, graphene nanoshell, photonic crystal, chemical potential, gate voltage, plane wave expansion method, finite-difference time-domain method

Posted Date: May 13th, 2021

DOI: https://doi.org/10.21203/rs.3.rs-475933/v1

Ultra-fast tunable optoelectronic full-adder based on photonic crystal ring resonators covered by graphene nanoshells

SALEH NAGHIZADE[1] AND HAMED SAGHAEI[2,*]

[1]Young Researchers and Elite Club, Tabriz Branch, Islamic Azad University, Tabriz, Iran
[2]Department of Electrical Engineering, Shahrekord Branch, Islamic Azad University, Shahrekord, Iran
*Corresponding Author: h.saghaei@iaushk.ac.ir

Abstract: This paper reports a new design of a tunable optoelectronic full-adder using two photonic crystal ring resonators (PCRRs). Every PCRR consists of a matrix of silicon rods surrounded by silica rods covered with graphene nanoshells (GNSs). The proposed full-adder is formed by three input ports, two PCRRs, and two output ports for 'SUM' and 'CARRY'. The plane wave expansion technique is used to study the photonic band structure of the fundamental PC microstructure, and the finite-difference time-domain method is also employed in the final design for solving Maxwell's equations to analyze the light propagation inside the structure. We can tune the PhC resonant mode for our desired application by setting the chemical potential of GNSs with an appropriate gate voltage. The numerical results reveal that when the chemical potential of GNSs changes, the switching mechanism occurs and manages the coupling and propagation direction of the input beam inside the structure. We systematically study the effects of physical parameters on the transmission, reflection, and absorption spectra. Our numerical results also demonstrate that the maximum delay is about 0.8 ps. The 663 μm^2 area of the proposed full-adder based on two-dimensional materials makes it a building block of every photonic integrated circuit used for data processing systems.

Keywords: Full-adder, graphene nanoshell, photonic crystal, chemical potential, gate voltage, plane wave expansion method, finite-difference time-domain method.

1. Introduction

Optoelectronics is the use of electronic devices to detect and control light as desired [1]. It is usually considered a subset of photonics or electronics and has applications in the electrical-to-optical and optical-to-electrical converters [2]. High-speed signal processing is very important for optical systems and networks, and optical communication technology introduces all-optical structures for this purpose. All-optical logic gates and combinational circuits are the basic building blocks for optical signal processing systems [3–6]. An optical full-adder as a computational operator must exist in every basic calculator [7–12]. Every full-adder consists of three input ports and two output ports. Therefore, the three binary numbers are added together, and the two binary numbers are obtained on the output side called 'SUM' and 'CARRY' [13]. One of the most challenging issues for optical designers is choosing a compact structure to confine the electromagnetic wave and transmit it to the desired output. Compared to solid-state crystals, photonic crystals (PhCs) become a powerful platform for the development of optical devices due to their photonic band gap (PBG), which leads to the emission of the optical beam through the desired waveguide [14]. Researchers have proposed various materials to integrate photonic circuits such as InP, GaAs, silicon on silicon dioxide

(SiO_2) as an insulator [15–17]. SiO_2 has negligible loss and low thermal sensitivity in the near-infrared wavelength range [18–20]. Photonic crystal ring resonators (PCRR) are well-known structures because they have excellent characteristics in realizing various compact optical devices [21–25]. Resonant modes of a PCRR depends on several physical parameters such as rod radius, lattice constant, and rods' refractive index [26–31]. In recent reports, researchers have shown that a PCRR can be used as an optical filter, and blueshift or redshift may occur in the resonant mod by changing any of these parameters [13,23]. So far, many PhC-based devices such as optical filters [32–35], logic gates [36–38], encoders [39–41], comparators [42,43], adders and subtractors [44–46], and switches [47–49] have been designed and investigated using PCRRs. Novel functionality of PCRR is proposed using nonlinear dielectric rods in the ring resonator [50,51]. This type of resonator can be used for filtering and switching applications. Recently all-optical half-adders and full-adders were designed using linear and nonlinear PhC structures [11,52,53]. The main drawback of all the proposed adders is their tunability. In other words, most of the proposed adders have PCRRs made of nonlinear rods, and the nonlinear phenomenon governing light propagation inside the PCRR is based on the optical Kerr effect. Thus, the intensity of the incoming light must be higher than a threshold value for this effect to appear. If this intensity exceeds a maximum value, it will damage the optical device [54]. Serajmohammadi et al. [55] used waveguides and ring resonators (RRs) inside the 2D hexagonal lattice of the PhC structure to realize an optical half-adder. The proposed structure works according to constructive and destructive interferences of optical waves. The 180-degree phase difference in inputs leads to destructive interference. For this purpose, different lengths of input waveguides in the XOR gate have been chosen. Their proposed structure has a delay time of 4 ps and a footprint of 1056 μm^2. Neisy et al. [53] proposed another optical half-adder consisting of two nonlinear resonant cavities (RCs). These RCs have different resonant modes due to the physical dimensions; therefore, their coupling operations depend on the power intensity. The proposed half-adder has a very short time response of 3ps. The main drawback of all studies is that half-adders are not tunable. Although few proposed logic gates are tunable based on the applied intensity, this tunability is limited to a special range of optical wavelengths. An ultrafast all-optical half-adder with a total footprint of 249.75 μm^2 was proposed by Hosseinzadeh Sani et al. [12]. Their structure contained two power regulators, two nonlinear ring resonators, and several waveguides. They used nonlinear rods in resonators; thus, the effective refractive index of the resonator changes as the intensity of incoming light changes. The desired resonance wavelength was tuned by adjusting the linear and nonlinear rods' radii. Their simulation results revealed that the delay time of their designed half-adder is about 3.6 ps. We designed a high-speed optical half-adder using PhC in an area of 158 μm^2 [56]. One of our structure's advantages compared to similar studies was the non-use of high nonlinear dielectric rods. This resulted in no need to increase the input power to divert the incoming light emission to the desired output. The calculations demonstrated that the proposed half-adder has a steady-state time of 0.8 ps due to its small area. Simulations revealed that the minimum transmission of logic 1 and the maximum transmission of logic 0 are 4% and 75%, respectively. However, the maximum transmission of 75% for logic 1 is not an ideal value. This is the first time, to our knowledge, we present a full-adder to overcome challenges mentioned above by designing a novel tunable structure capable of generating standard binary codes from an analog input. For this purpose, we employed a graphene nanoshell (GNS) in

PCRRs used in our structure. It is due to graphene's key characteristics, such as fast optical response, broadband window, high carrier mobility, excellent band structure, and unique mechanical strength and flexibility [1,57,58]. The rest of This paper is organized as follows. The full-adder's physical structure and the numerical results achieved by the plane wave expansion (PWE) method are presented in Section 2. Section 3 describes the light propagation inside the full-adder using the numerical finite-difference time-domain (FDTD) method and its functionality will be discussed, and the paper is closed by the conclusion in Section 4.

2. Design, model, and methods

2.1 Mathematical background

Graphene has electro-optic tunability, mechanical flexibility, high optical transmission efficiency, zero-band-gap (ZBG), and existing free electrons under zero doping conditions. All mentioned features result in this 2D material becoming a suitable material for fabricating highly tunable optoelectronic and plasmonic devices. In the range from infrared to terahertz, graphene supports a strong plasmonic response, which significantly increases light and graphene interaction. From the ultraviolet (UV) to near-infrared (NIR) wavelength range, monolayer graphene can only absorb a very small fraction of light due to the lack of plasmonic response in this region. It is about ~2.3% for the visible to NIR range and ~9% for the UV range [59]. According to the graphene sheet electron flexibility, the generation of certain Fermi energy band levels (E_f) can be obtained in the graphene layer by several methods such as adding substrate and biasing the gate voltage between the substrate and graphene layer. These methods permit us to modify the optical properties of graphene and the operating parameters of graphene-based optoelectronic devices, such as the central resonance wavelength and quality factor. The graphene sheet's optoelectronic features make it a popular candidate for designing integrated optoelectronic devices. In practice, research groups proposed integrating graphene on insulator substrates such as Si and SiO_2. In this work, the GNS with the thickness of d is deposited around the silica rod on the SiO_2 substrate. Charge carrier density (n_c) of a GNS on SiO_2 substrate can be tuned by applying the gate voltage (V_g) between the substrate and GNS. The charge carrier density is computed as the following equation [60,61]

$$n_c = \frac{V_g \varepsilon_0 \varepsilon_r}{eh} = V_g C \tag{1}$$

where ε_0 and ε are the air permittivity and substrate's relative permittivity, respectively. e and h are the electron charge and the substrate height. In Eq.1, the amount of $\varepsilon_0 \varepsilon_r / eh$ is equal to C, which is called the gate capacitance. The GNS chemical potential (μ_c) is calculated as follows [62,63]:

$$\mu_c = \hbar v_f \sqrt{\pi n_c} = \hbar v_f \sqrt{\pi V_g C} \tag{2}$$

where, $\hbar$ is the reduced Plank's constant and v_f is the Fermi velocity. The resonance wavelength of the GNS, λ_0, can be derived from the quasi-static analysis method as [64]:

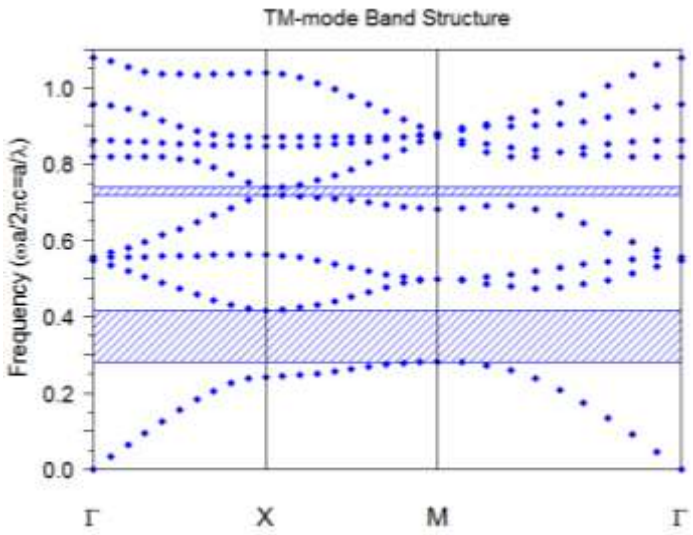

Fig. 1. The band structure diagram of fundamental PhC in TM mode.

$$\lambda_0 \approx \frac{2\pi c\hbar}{e}\sqrt{\frac{\varepsilon_{eff}\varepsilon_0 d\zeta}{E_f}} \tag{3}$$

where ε_{eff} is the effective permittivity of the medium surrounding the GNS that is $\varepsilon_{eff} = \left(\varepsilon_{SiO_2} + \varepsilon_0\right)/2$, and d is the thickness of GNS [65]. The dimensionless constant $\zeta = 3.1$ is a fitting parameter. The conductivity of a GNS (δ) at T=300^{0}k for infrared to THz frequencies is approximated using Drude-like expression as follows[35,66]

$$\delta \approx \frac{ie^2 E_f}{\pi\hbar^2\left(\omega + i\tau^{-1}\right)} \tag{4}$$

where τ and ω are the electron relaxation time and the angular frequency, respectively. Also, when the number of GNS layer (N) is more than one, the conductivity for N-layer GNS will be Nδ. Recently, published papers showed that the finite-difference time-domain (FDTD) method is a comprehensive technique to study the propagation of electromagnetic waves inside compact optical devices such as PhC-based structures. This method solves Maxwell's equation in a tiny volume of the intended PhC device [67,68]. In this study, the plane wave expansion (PWE) method calculates the PBG region. The FDTD method is also used to solve Maxwell's equation and study the waveguide's light propagation. The following equation gives the optical absorption of graphene [69]

$$A(\lambda) = \frac{4\pi c}{\lambda} n(\lambda) k(\lambda) \int_V |E_l|^2 dV \tag{5}$$

where c is the speed of light and in free space, V is the graphene volume, and E_l is the local electric field. According to Eq. (5), the light absorption is proportional to the square of local electric field intensity. The UV absorption in graphene is significantly increased at $\lambda = 273$ nm due to the large increase in the electric field.

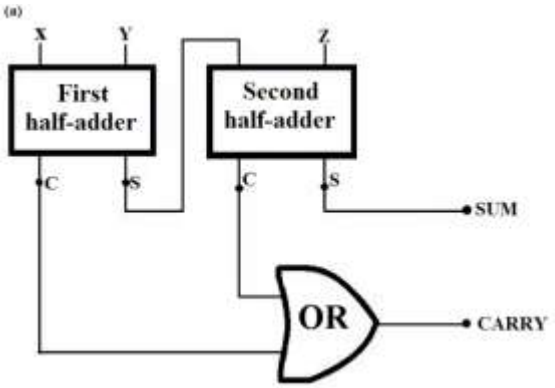

(b)

INPUT			OUTPUT	
X	Y	Z	SUM	CARRY
0	0	0	0	0
0	0	1	1	0
0	1	0	1	0
0	1	1	0	1
1	0	0	1	0
1	0	1	0	1
1	1	0	0	1
1	1	1	1	1

Fig. 2. Illustration of (a) the typical full-adder circuit formed by two half-adders and an OR logic gate, three input ports of A, B, and Z, and two output ports of SUM and CARRY, (b) the truth table of full-adder for all states.

2.2 Optoelectronic full-adder

The fundamental 2D PhC used in this study has a square lattice of dielectric rods. The rod radius is 118 nm, and the refractive index of silicon rods is assumed to be 3.46. The plane wave expansion (PWE) method has been employed to calculate the photonic band structure. Figure 1 shows the fundamental PhC has two PBG regions in TM mode where the first one is at 0.29 $<a/\lambda<$ 0. 0.41. In this study, the lattice constant is assumed to be a=590 nm; therefore, an optical beam with a wavelength of 1439 nm $<\lambda<$ 2034 nm cannot propagate in any PhC direction. By removing several dielectric rods in the fundamental PhC structure, a waveguide can be created. Accordingly, the wavelengths in the PBG region can be propagated in this waveguide. Figure 2(a) shows a typical full-adder consisting of three input ports (labeled as X, Y, and Z) and two output ports, called SUM and CARRY. As seen, a full-adder is made by combining two half-adders and one OR logic gate. Every half-adder consists of two input ports and two output ports of S and C used for SUM and CARRY, respectively. X and Y are the input ports of the first half-adder, and S and Z are the input ports of the second half-adder. The first half-adder output port, S, has been connected to the first input port of the second half-adder. C ports of optical half-adders are the inputs of the OR logic gate, and its output is the CARRY of the final full-adder and S output port of the second half-adder is the SUM port of the proposed full-adder. Besides, A, B, and Z are the three input ports of the full-adder. Figure 2(b) represents the truth table of a typical full-adder. As shown in the figure, when three inputs are inactive (logic 0 is used for OFF state), i.e., no signal is applied to them, or the amplitude of the input signals is less than a threshold value, then both output ports turn OFF. If only one input port is turned ON (logic 1 is used for ON mode), SUM is activated, and CARRY turns OFF. If only two input ports are active, SUM turns OFF, and CARRY turns ON, and when all input ports are active, SUM and CARRY turn ON. For the GNS-based PCRR design, we replace several silicon dielectric rods with silica rods in the outer ring of the resonator. The rods radius (r) and linear refractive index of silica are 108 nm and 1.4, respectively. Moreover, the SiO_2 defect rods are surrounded by the GNSs with a thickness of 10 nm.

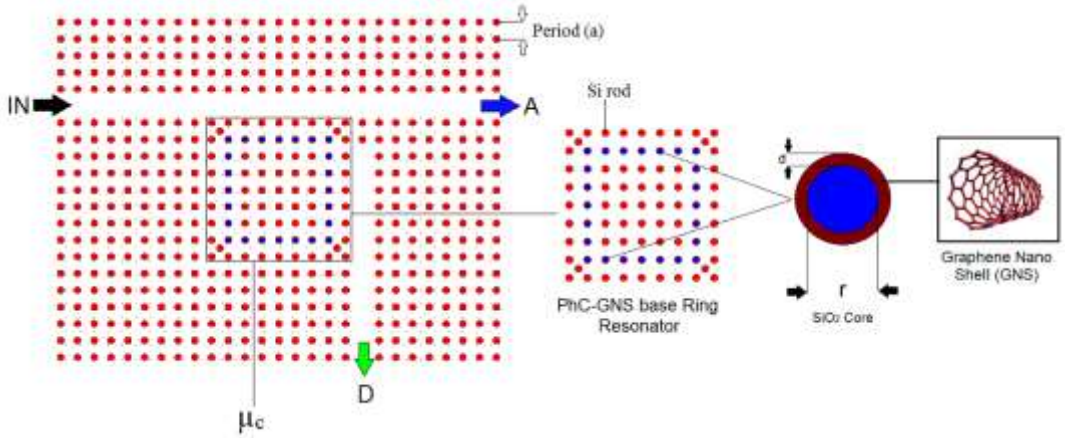

Fig. 3. The schematic view of GNS-based PhC ring resonator and corresponding waveguides.

Figure 3 demonstrates the proposed PCRR, where GNS material and silica defect rods are shown in dark red and blue colors, respectively. As seen, the proposed PCRR consists of one input port, and two output ports called A and D.

An optical beam centered at 1550nm with an amplitude of 1V/m is launched into the input waveguide and dropped to the PCRR. The signal output of the PCRR depends on the value of GNS chemical potential (μ_c). The time-domain light propagation inside the PCRR for two different values of μc are shown in Figs. 4(a), and 4(b). As shown in Fig. 4(b), when the μc set to 0.5ev, the optical beam enters the resonator and is guided to the output port of D, and the measured power is more than 80%.

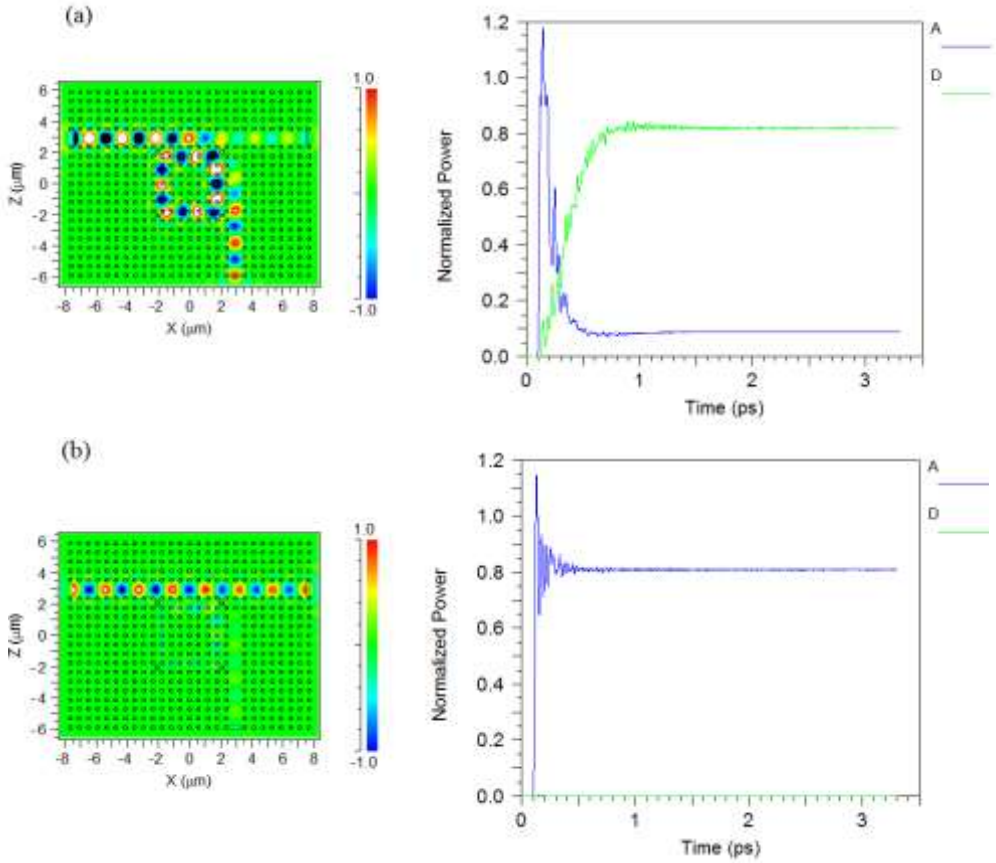

Fig. 4. Light propagation inside the GNS base PhCRR for different values of μc (a) μc =0.5ev and (b) μc=0.3ev.

when the μc set to 0.3ev, the optical beam doesn't enter the resonator and exits the output port A with an optical power of 80%. As shown in Fig. 5, the proposed full-adder consists of eight waveguides and two GNS-based ring resonators in appropriate locations within the initial PhC structure. The W1, W2, W3, and W6 waveguides and the R1 resonator with a chemical potential of μc_1 form the first half-adder. The S and C ports of the first half-adder are placed at the right side of W3 and W6. Also, the waveguides W4, W5, and W7 and resonator R2 with a chemical potential of μc_2 form the second half-adder. The S and C ports of the second half-adder are to the right of the W5 and W7 waveguides. W6, W7, and W8 form the OR gate, and W8 is used as the CARRY port of the proposed full-adder. Also, the right side of the W5 works as the SUM output port, and X, Y, and Z are defined as the input ports of the proposed full-adder. For more clarity, the three-dimensional view of the proposed full-adder is shown in Fig. 5 (b) where the SiO_2 plate shown in gray is the substrate with a thickness of h= 2 μm. Gate voltages of V1 and V2 are applied to the first and second GNS-based PCRRs, respectively, to tune the output states of the proposed full-adder by changing the values of μc in both ring resonators.

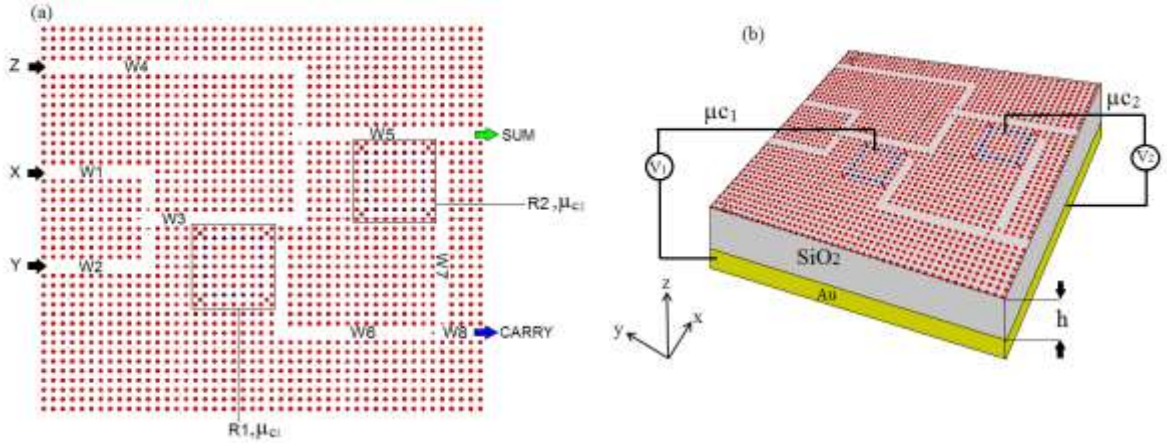

Fig. 5. Illustration of the proposed full-adder, (a) top view of XY plane, and (b) the perspective view.

3. Simulation and Results

Using the FDTD method, we analyze and simulate the light propagation inside the proposed full-adder consisting of three input ports of X, Y, and Z. Therefore, according to the computational principle, we have 2^3 (2^N, N is the number of input ports) different input states and an optical signal centered at 1550nm with an amplitude of 1V/m is launched into every active input port. The simulation results are discussed as follows for all eight states of input ports.

Case #1: When all the input ports X, Y, and Z are inactive, meaning that the signal strength applied to them is negligible, no light beam enters the structure. Therefore, there is no optical signal in the full-adder, and both output ports are OFF. It means that the amounts of SUM and CARRY are assumed to be zero.

Case #2: When X=1, Y=0, and Z=0, we set the μc_1 to 0.3ev by biasing the V_1. Therefore, electromagnetic waves coming from input port X travel close to R1 through W1 and W3. Since

the μc_1 is less than 0.5ev, the optical signal will be guided into W5 using W3 and reached R2., The optical beam doesn't drop into R2 and travels toward the SUM port because we set the μc_2 to 0.3ev by biasing the V_2. Therefore, the output port corresponding to SUM will be active (SUM =1), and the output port corresponding to CARRY remains inactive (CARRY=0). Figure 6(a) demonstrates the light propagation inside the proposed full-adder, and Fig. 6(b) shows that the output powers at SUM and CARRY output ports are about 75% and 5% of the input power, respectively, which is called the normalized power. Also, the time delay is about 0.8 ps. It is the time that the device needs to reach a steady state.

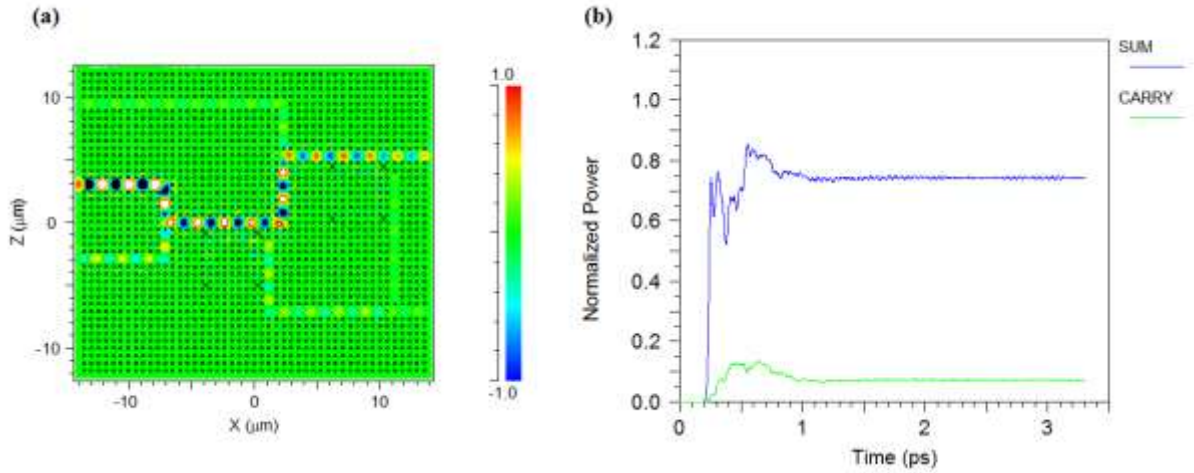

Fig. 6. Illustration of (a) Light emission distribution and (b) normalized powers of the proposed optoelectronic full-adder using GNS-based PCRRs for Case #2.

Case #3: When X=0, Y=1, and Z=0, we set the μc_1 to 0.3ev by biasing the V_1. Figure 7(a) demonstrates that the electromagnetic waves coming from input port Y travel close to R1 through W2 and W3. Since the μc_1 is less than 0.5ev, the optical signal will be guided into W5 using W3 and reached R2. Similar to Case #2, the optical beam doesn't drop into resonator R2 and travels toward the SUM port because we set the μc_2 to 0.3ev by biasing the V_2. Therefore, we will have SUM=1 and CARRY=0. Figure 7(b) illustrates that the normalized powers at SUM and CARRY are more than 75% and less than 5%, respectively. Also, the time delay is about 0.8 ps.

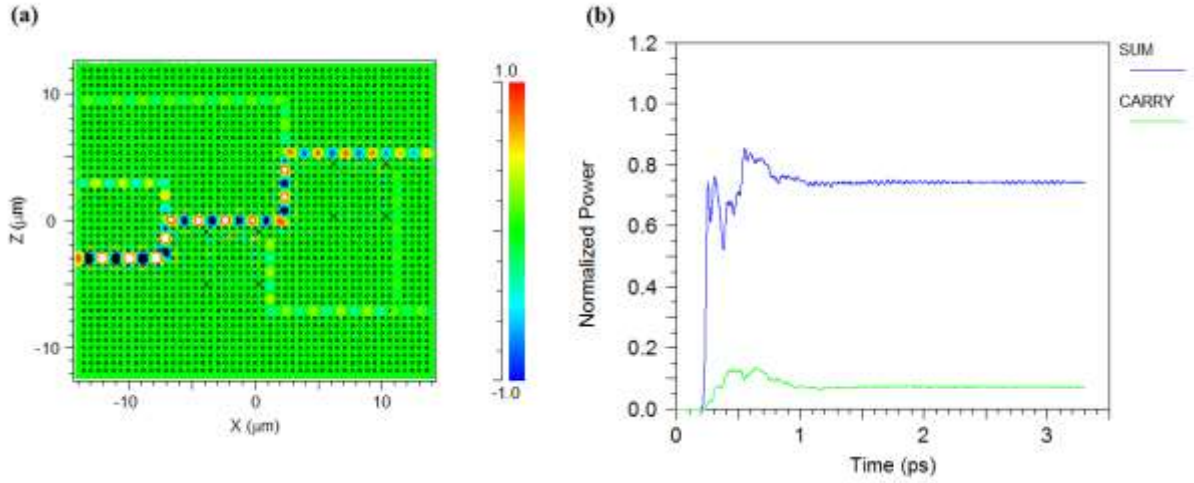

Fig. 7. Illustration of (a) Light emission distribution and (b) normalized powers of the proposed optoelectronic full-adder using GNS-based PCRRs for Case #3.

Case #4: When X=0, Y=0, and Z=1, we set the μc_2 to 0.3ev by biasing the V_2. Therefore, electromagnetic waves coming from input port Z travel close to R2 through W4 and W5. The optical beam doesn't drop into R2 and travels toward the SUM port because we set the μc_2 to 0.3ev by biasing the V_2. Therefore, the SUM will be active (SUM =1), and CARRY remains inactive (CARRY=0). Figure 8(a) demonstrates the light propagation inside the proposed full-adder, and Fig. 8(b) shows that the normalized output powers of SUM and CARRY are more than 80% and less than 2%, respectively. Also, the time delay is about 0.8 ps.

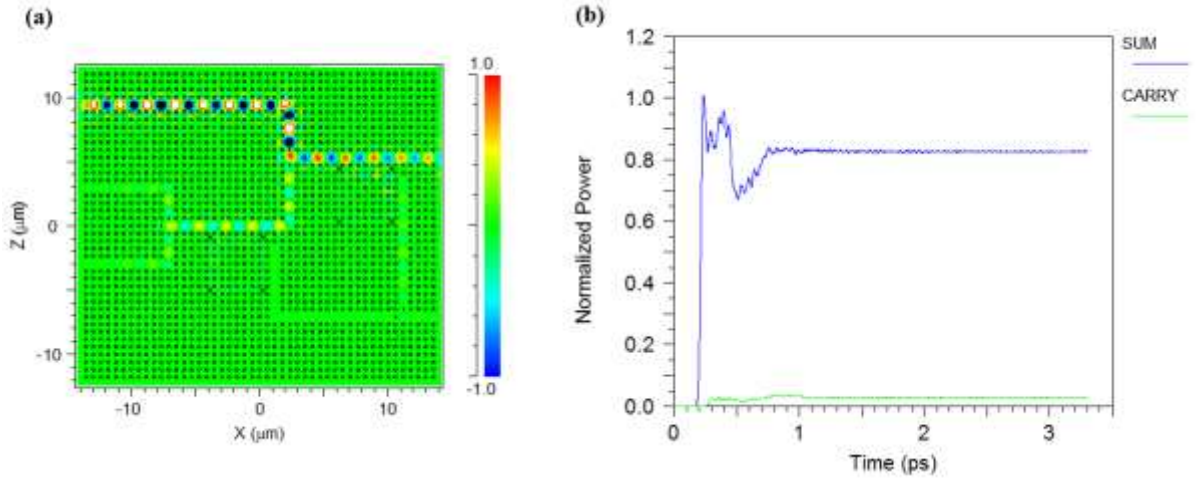

Fig. 8. Illustration of (a) Light emission distribution and (b) normalized powers of the proposed optoelectronic full-adder using GNS-based PCRRs for Case #4.

Case #5: When X=1, Y=0, and Z=1, we set the μc_1 to 0.3ev by biasing the V_1. As shown in Fig. 9(a), the electromagnetic waves coming from input port X travel close to R1 through W1 and W3. Since μc_1 is less than 0.5ev, the optical signal doesn't drop into R1 and emits toward W5 using W3 and reaches R2. Also, electromagnetic waves coming from input port Z travels close to R2 through W4 and W5. By biasing V_2, we set the μc_2 to 0.5ev; thus, the optical beam drops into R2 and guides toward the W7 port and reaches to OR gate. In this case, we have SUM=0 and CARRY=1. Figure 9(b) shows that the normalized powers at SUM and CARRY are less than 3% and less than 140%, respectively. Also, the time delay is about 0.8 ps.

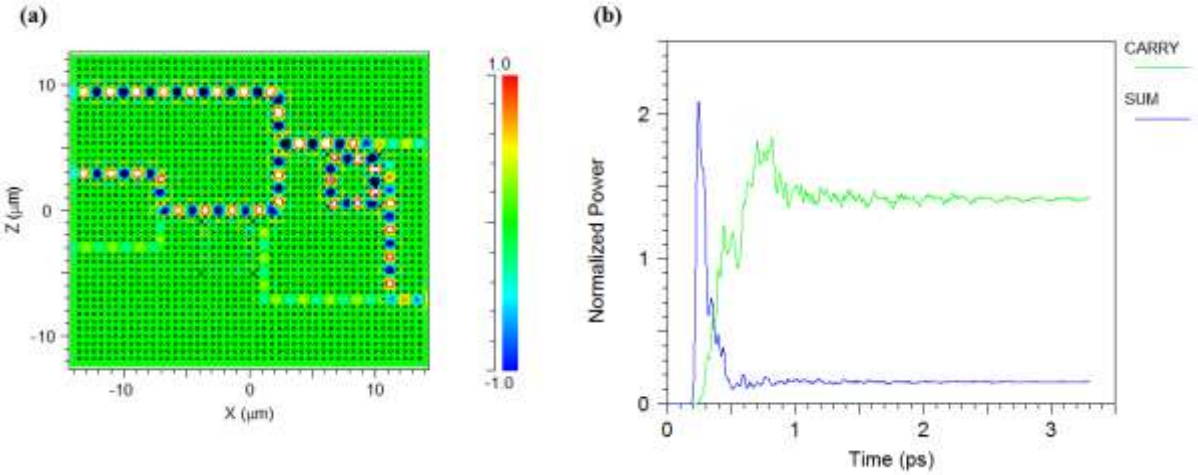

Fig. 9. Illustration of (a) Light emission distribution and (b) normalized powers of the proposed optoelectronic full-adder using GNS-based PCRRs for Case #5.

Case #6: When X=0, Y=1, and Z=1, we set the μc_1 to 0.3ev by biasing the V_1. As seen in Fig. 10(a), the electromagnetic waves coming from input port Y travels close to R1 through W2 and W3. Since μc_1 is less than 0.5ev, the optical signal doesn't drop into R1 and will be propagated to W5 using W3 and reaches R2. Also, electromagnetic waves coming from input port Z travels close to R2 through W4 and W5. In this condition, by biasing the V2, we set the μc_2 to 0.5ev, the optical beam drops into R2 and guides toward the W7 port, and reaches to OR gate. Thus, we have SUM=0 and CARRY=1. Figure 10(b) shows that the normalized powers at SUM and CARRY are less than 3% and more than 140%, respectively. Also, the time delay is about 0.8 ps.

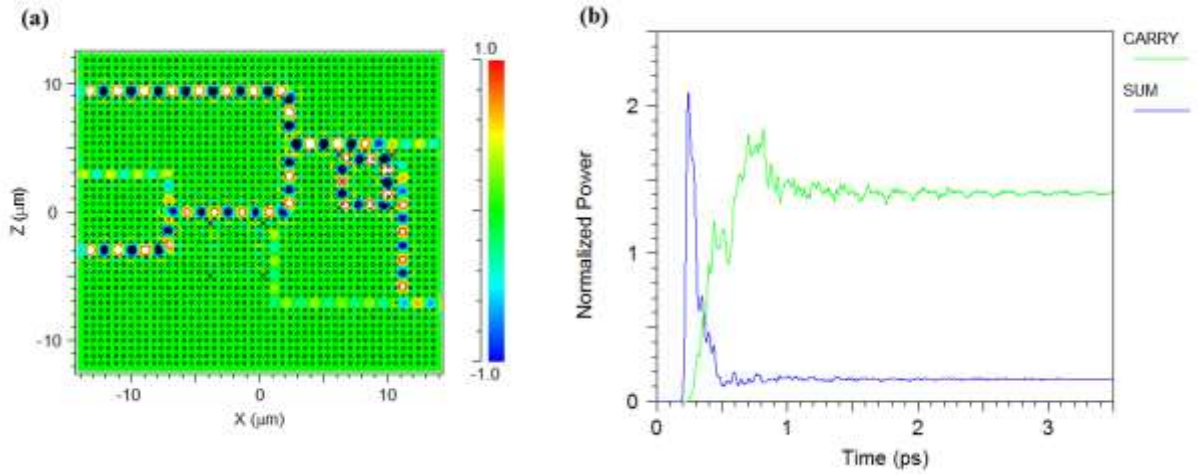

Fig. 10. Illustration of (a) Light emission distribution and (b) normalized powers of the proposed optoelectronic full-adder using GNS-based PCRRs for Case #6.

Case #7: When X=1, Y=1, and Z=0, we set the μc_1 to 0.5ev by biasing the V_1. Therefore, electromagnetic waves coming from input port X travel close to R1 through W1 and W3. Also, electromagnetic waves coming from input port Y travels close to R1 through W2 and W3. Consequently, the optical signal drops into R1 and will be guided into W6 and reaches the OR gate. Thus, we have SUM=0 and CARRY=1.

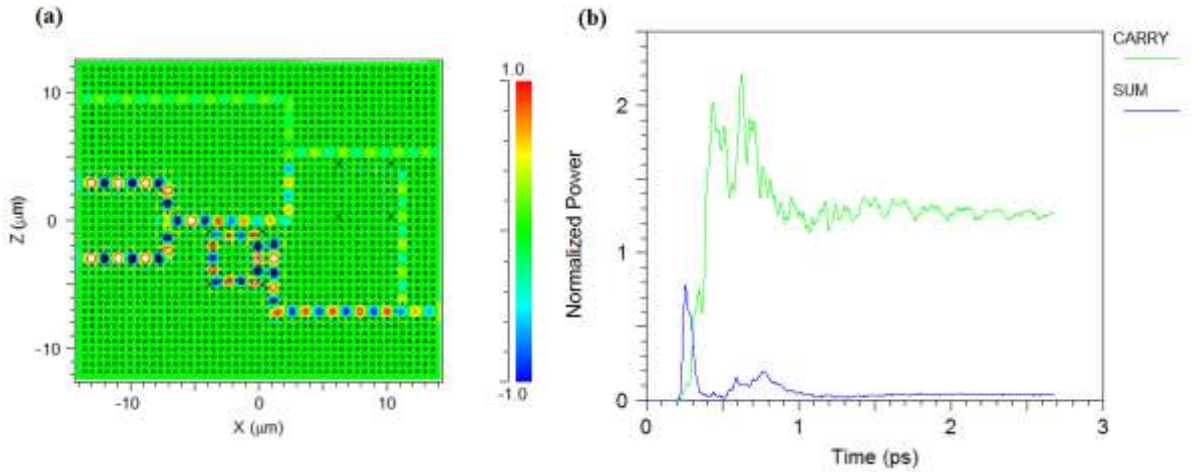

Fig. 11. Illustration of (a) Light emission distribution and (b) normalized powers of the proposed optoelectronic full-adder using GNS-based PCRRs Case #7.

Figure 11(a) shows The distribution of light propagation inside the proposed structure, and Fig. 11 (b) shows that the normalized powers at SUM and CARRY are less than 1% and more than 130%, respectively. Also, the time delay is about 0.8 ps.

Case #8: When X=1, Y=1, and Z=1, we set the μc_1 to 0.5ev by biasing the V1. Therefore, electromagnetic waves coming from input port X travel close to R1 through W1 and W3. Also, electromagnetic waves coming from input port Y travels close to R1 through W2 and W3. Consequently, the optical signal drops into R1 and will be guided into W6 and reaches the OR gate. Furthermore, optical beams coming from input port Z travels close to R2 through W4 and W5. Biasing the V1, we set the μc_1 to 0.5ev; thus, the optical beam coming from port Z doesn't drop into R2 and travels toward the SUM port. In this case, we have SUM=1 and CARRY=1. The proposed full adder's light propagation is demonstrated in Fig. 12(a). The normalized powers at SUM and CARRY are more than 75% and 120%, respectively (See Fig. 12(b)). Also, time delays are approximately 0.8 ps for both CARRY and SUM.
All eight input states and corresponding outputs are summarized in Table 1. It shows that the proposed structure is working as a full-adder.

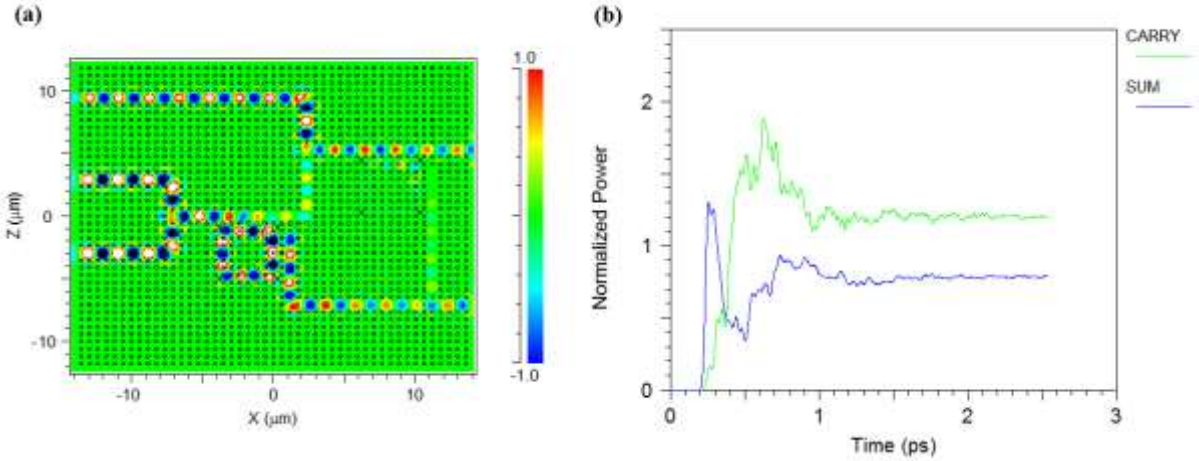

Fig. 12. Illustration of (a) Light emission distribution and (b) normalized powers of the proposed optoelectronic full-adder using GNS-based PCRRs for Case #8.

Table 1: The proposed full adder's outputs for different input states.

Case	Input			Normalized Outputs (%)		Logic Levels	
	X	Y	Z	SUM	CARRY	SUM	CARRY
#1	0	0	0	0	0	0	0
#2	1	0	0	75	7	1	0
#3	0	1	0	75	7	1	0
#4	0	0	1	80	2	1	0
#5	1	0	1	3	140	0	1
#6	0	1	1	3	140	0	1
#7	1	1	0	1	130	0	1
#8	1	1	1	75	120	1	1

4. Conclusion

In summary, we designed an ultra-fast tunable optoelectronic full-adder based on photonic crystal ring resonators covered by graphene nanoshells. The presented structure consisted of

eight waveguides, two GNS-based ring resonators, three input ports, and two output ports. Eight different states for three input ports were simulated and discussed. The numerical results revealed that the proposed structure can be tuned by changing the chemical potential of GNS material in every ring resonator. The proposed structure can be used as an optoelectronic full-adder with a maximum delay of about 0.8ps. Thus, it is an appropriate device for high-speed data processing systems.

Funding
This research received no specific grant from any funding agency in the public, commercial, or not-for-profit sectors.

Disclosures
The authors declare no conflicts of interest.

References

1. Z. Sun, A. Martinez, en F. Wang, "Optical modulators with 2D layered materials," Nat. Photonics **10**(4), 227–238 (2016).
2. Q. Bao en K. P. Loh, "Graphene photonics, plasmonics, and broadband optoelectronic devices," ACS Nano **6**(5), 3677–3694 (2012).
3. H. Sharifi, S. M. Hamidi, en K. Navi, "A new design procedure for all-optical photonic crystal logic gates and functions based on threshold logic," Opt. Commun. **370**, 231–238 (2016).
4. A. Rahmani en F. Mehdizadeh, "Application of nonlinear PhCRRs in realizing all optical half-adder," Opt. Quantum Electron. **50**(1), 30 (2018).
5. H. Saghaei, A. Zahedi, R. Karimzadeh, en F. Parandin, "Line defects on photonic crystals for the design of all-optical power splitters and digital logic gates," Superlattices Microstruct. **110**, 133–138 (2017).
6. S. Wabnitz en B. J. Eggleton, "All-optical signal processing," Data Commun. Storage Appl. (2015).
7. M. J. Maleki, A. Mir, en M. Soroosh, "Designing an ultra-fast all-optical full-adder based on nonlinear photonic crystal cavities," Opt. Quantum Electron. **52**(4), 1–11 (2020).
8. A. M. Vali-Nasab, A. Mir, en R. Talebzadeh, "Design and simulation of an all optical full-adder based on photonic crystals," Opt. Quantum Electron. **51**(5), (2019).
9. F. Cheraghi, M. Soroosh, en G. Akbarizadeh, "An ultra-compact all optical full adder based on nonlinear photonic crystal resonant cavities," Superlattices Microstruct. **113**, 359–365 (2018).
10. Q. Liu en Z. B. Ouyang, "All-optical half adder based on cross structures in two-dimensional photonic crystals," Guangzi Xuebao/Acta Photonica Sin. **37**(SUPPL. 2), 46–50 (2008).
11. Y. C. Jiang, S. Bin Liu, H. F. Zhang, en X. K. Kong, "Realization of all optical half-adder based on self-collimated beams by two-dimensional photonic crystals," Opt. Commun. **348**, 90–94 (2015).
12. M. H. Sani, A. A. Tabrizi, H. Saghaei, en R. Karimzadeh, "An ultrafast all-optical half adder using nonlinear ring resonators in photonic crystal microstructure," Opt. Quantum Electron. **52**(2), 107 (2020).
13. S. Naghizade en H. Saghaei, "A novel design of all-optical full-adder using nonlinear X-shaped photonic crystal resonators," Opt. Quantum Electron. **53**(3), 1–13 (2021).
14. E. Yablonovitch, "Photonic band-gap structures," J. Opt. Soc. Am. B **10**(2), 283 (1993).
15. I. Calizo, W. Bao, F. Miao, C. N. Lau, en A. A. Balandin, "The effect of substrates on the Raman spectrum of graphene: Graphene- on-sapphire and graphene-on-glass," Appl. Phys. Lett. **91**(20), 201904 (2007).
16. M. Danaie en H. Kaatuzian, "Bandwidth Improvement for a Photonic Crystal Optical Y-splitter," J. Opt. Soc. Korea **15**(3), 283–288 (2011).
17. G. Roelkens, J. Brouckaert, D. Taillaert, P. Dumon, W. Bogaerts, D. Van Thourhout, R. Baets, R. Nötzel, en M. Smit, "Integration of InP/InGaAsP photodetectors onto silicon-on-insulator waveguide circuits," Opt. Express **13**(25), 10102 (2005).
18. K. S. Song en R. T. Williams, "Silicon Dioxide," in *Handbook of optical constants of solids* (Elsevier, 1993), bll 270–299.
19. M. Ebnali-Heidari, H. Saghaei, F. Koohi-Kamali, M. Naser Moghadasi, en M. K. Moravvej-Farshi, "Proposal for Supercontinuum Generation by Optofluidic Infiltrated Photonic Crystal Fibers," IEEE J. Sel. Top. Quantum Electron. **20**(5), (2014).
20. M. Ebnali-Heidari, F. Dehghan, H. Saghaei, F. Koohi-Kamali, en M. K. Moravvej-Farshi, "Dispersion engineering of photonic crystal fibers by means of fluidic infiltration," J. Mod. Opt. **59**(16), 1384–1390 (2012).

21. M. R. Rakhshani en M. A. Mansouri-Birjandi, "Design and simulation of four-channel wavelength demultiplexer based on photonic crystal circular ring resonators for optical communications," J. Opt. Commun. **35**(1), 9–15 (2014).
22. F. Mehdizadeh, M. Soroosh, en H. Alipour-Banaei, "An optical demultiplexer based on photonic crystal ring resonators," Optik (Stuttg). **127**(20), 8706–8709 (2016).
23. F. Mehdizadeh, M. Soroosh, en H. Alipour-Banaei, "A novel proposal for optical decoder switch based on photonic crystal ring resonators," Opt. Quantum Electron. **48**(1), 1–9 (2016).
24. H. Alipour-Banaei, F. Mehdizadeh, en S. Serajmohammadi, "A novel 4-channel demultiplexer based on photonic crystal ring resonators," Optik (Stuttg). **124**(23), 5964–5967 (2013).
25. M. Djavid, A. Ghaffari, F. Monifi, en M. S. Abrishamian, "T-shaped channel-drop filters using photonic crystal ring resonators," Phys. E Low-dimensional Syst. Nanostructures **40**(10), 3151–3154 (2008).
26. A. Tavousi, M. A. Mansouri-Birjandi, M. Ghadrdan, en M. Ranjbar-Torkamani, "Application of photonic crystal ring resonator nonlinear response for full-optical tunable add–drop filtering," Photonic Netw. Commun. **34**(1), 131–139 (2017).
27. M. A. Mansouri-Birjandi, A. Tavousi, en M. Ghadrdan, "Full-optical tunable add/drop filter based on nonlinear photonic crystal ring resonators," Photonics Nanostructures - Fundam. Appl. **21**, 44–51 (2016).
28. U. Biswas, J. K. Rakshit, en G. K. Bharti, "Design of photonic crystal microring resonator based all-optical refractive-index sensor for analyzing different milk constituents," Opt. Quantum Electron. **52**(1), 19 (2020).
29. A. Farmani, M. Soroosh, M. H. Mozaffari, en T. Daghooghi, "Optical nanosensors for cancer and virus detections," in *Nanosensors for Smart Cities* (Elsevier, 2020), bll 419–432.
30. S. Naghizade, S. Mohammadi, en H. Khoshsima, "Design and simulation of an all optical 8 to 3 binary encoder based on optimized photonic crystal or gates," J. Opt. Commun. **410**, 793–798 (2018).
31. S. Naghizade en S. M. Sattari-Esfahlan, "Loss-less elliptical channel drop filter for WDM applications," J. Opt. Commun. **40**(4), 379–384 (2017).
32. Y. Guo, S. Zhang, J. Li, S. Li, en T. Cheng, "A sensor-compatible polarization filter based on photonic crystal fiber with dual-open-ring channel by surface plasmon resonance," Optik (Stuttg). **193**, 162868 (2019).
33. H. Alipour-Banaei, M. Jahanara, en F. Mehdizadeh, "T-shaped channel drop filter based on photonic crystal ring resonator," Optik (Stuttg). **125**(18), 5348–5351 (2014).
34. M. R. Rakhshani en M. A. Mansouri-Birjandi, "Realization of tunable optical filter by photonic crystal ring resonators," Optik (Stuttg). **124**(22), 5377–5380 (2013).
35. S. Naghizade en H. Saghaei, "Tunable graphene-on-insulator band-stop filter at the mid-infrared region," Opt. Quantum Electron. **52**(4), 224 (2020).
36. R. M. Younis, N. F. F. Areed, en S. S. A. Obayya, "Fully integrated and and or optical logic gates," IEEE Photonics Technol. Lett. **26**(19), 1900–1903 (2014).
37. P. Andalib en N. Granpayeh, "All-optical ultracompact photonic crystal AND gate based on nonlinear ring resonators," J. Opt. Soc. Am. B **26**(1), 10 (2009).
38. H. M. E. Hussein, T. A. Ali, en N. H. Rafat, "New designs of a complete set of Photonic Crystals logic gates," Opt. Commun. **411**, 175–181 (2018).
39. S. Naghizade en H. Khoshsima, "Low input power an all optical 4×2 encoder based on triangular lattice shape photonic crystal," J. Opt. Commun. **1**, 1–8 (2018).
40. T. A. Moniem, "All-optical digital 4 × 2 encoder based on 2D photonic crystal ring resonators," J. Mod. Opt. **63**(8), 735–741 (2016).
41. S. Naghizade en H. Saghaei, "A novel design of all-optical 4 to 2 encoder with multiple defects in silica-based photonic crystal fiber," Optik (Stuttg). **222**, 165419 (2020).
42. V. Fakouri-Farid en A. Andalib, "Design and simulation of an all optical photonic crystal-based comparator," Optik (Stuttg). **172**, 241–248 (2018).
43. H. Jile, "Realization of an all-optical comparator using beam interference inside photonic crystal waveguides," Appl. Opt. **59**(12), 3714 (2020).
44. M. Hosseinzadeh Sani, A. Ghanbari, en H. Saghaei, "An ultra-narrowband all-optical filter based on the resonant cavities in rod-based photonic crystal microstructure," Opt. Quantum Electron. **52**(6), 295 (2020).
45. R. Moradi, "All optical half subtractor using photonic crystal based nonlinear ring resonators," Opt. Quantum Electron. **51**(4), 119 (2019).
46. H. Alipour-Banaei en H. Seif-Dargahi, "Photonic crystal based 1-bit full-adder optical circuit by using ring resonators in a nonlinear structure," Photonics Nanostructures-Fundamentals Appl. **24**, 29–34 (2017).
47. M. Ghadrdan en M. A. Mansouri-Birjandi, "Low-threshold ultrafast all-optical switch implemented with metallic nanoshells in the photonic crystal ring resonator," Superlattices Microstruct. **111**, 789–795 (2017).
48. M. Radhouene, M. Najjar, M. K. Chhipa, S. Robinson, en B. Suthar, "Design and analysis a thermo-optic switch based on photonic crystal ring resonator," Optik (Stuttg). **172**, 924–929 (2018).
49. R. Rajasekar, K. Parameshwari, en S. Robinson, "Nano-optical switch based on photonic crystal ring resonator," Plasmonics **14**(6), 1687–1697 (2019).

50. T. Daghooghi, M. Soroosh, en K. Ansari-Asl, "A low-power all optical decoder based on photonic crystal nonlinear ring resonators," Optik (Stuttg). **174**, 400–408 (2018).
51. A. Foroughifar, H. Saghaei, en E. Veisi, "Design and analysis of a novel four-channel optical filter using ring resonators and line defects in photonic crystal microstructure," Opt. Quantum Electron. **53**(2), 101 (2021).
52. M. Ghadrdan en M. A. Mansouri-Birjandi, "Concurrent implementation of all-optical half-adder and AND & XOR logic gates based on nonlinear photonic crystal," Opt. Quantum Electron. **45**(10), 1027–1036 (2013).
53. M. Neisy, M. Soroosh, en K. Ansari-Asl, "All optical half adder based on photonic crystal resonant cavities," Photonic Netw. Commun. **35**(2), 245–250 (2018).
54. C. W. Carr, H. B. Radousky, A. M. Rubenchik, M. D. Feit, en S. G. Demos, "Localized Dynamics during Laser-Induced Damage in Optical Materials," Phys. Rev. Lett. **92**(8), 87401 (2004).
55. S. Serajmohammadi, H. Alipour-Banaei, en F. Mehdizadeh, "Proposal for realizing an all-optical half adder based on photonic crystals," Appl. Opt. **57**(7), 1617–1621 (2018).
56. S. Naghizade en H. Saghaei, "A Novel Design of All-Optical Half-Adder Using a Linear Defect in Photonic Crystal Microstructure," J. Appl. Res. Electr. Eng. (2020).
57. R. Tang, S. Han, F. Teng, K. Hu, Z. Zhang, M. Hu, en X. Fang, "Size-Controlled Graphene Nanodot Arrays/ZnO Hybrids for High-Performance UV Photodetectors," Adv. Sci. **5**(1), 1700334 (2018).
58. L. Ye, Y. Chen, G. Cai, N. Liu, J. Zhu, Z. Song, en Q. H. Liu, "Broadband absorber with periodically sinusoidally-patterned graphene layer in terahertz range," Opt. Express **25**(10), 11223–11232 (2017).
59. R. R. Nair, P. Blake, A. N. Grigorenko, K. S. Novoselov, T. J. Booth, T. Stauber, N. M. R. Peres, en A. K. Geim, "Fine structure constant defines visual transparency of graphene," Science (80-.). **320**(5881), 1308 (2008).
60. T. T. M. Thi, P. T. Dat, V. C. Minh, N. H. Tho, en N. X. Sang, "Physical Adsorption and Photocatalytic Activity of Titanium Dioxide Nanotube and Graphene Oxide Composite," VNU J. Sci. Nat. Sci. Technol. **34**(3), (2018).
61. B. Shi, W. Cai, X. Zhang, Y. Xiang, Y. Zhan, J. Geng, M. Ren, en J. Xu, "Tunable band-stop filters for graphene plasmons based on periodically modulated graphene," Sci. Rep. **6**(1), 1–7 (2016).
62. L. Ju, B. Geng, J. Horng, C. Girit, M. Martin, Z. Hao, H. A. Bechtel, X. Liang, A. Zettl, Y. R. Shen, en F. Wang, "Graphene plasmonics for tunable terahertz metamaterials," Nat. Nanotechnol. **6**(10), 630–634 (2011).
63. A. Farmani, M. Miri, en M. H. Sheikhi, "Analytical modeling of highly tunable giant lateral shift in total reflection of light beams from a graphene containing structure," Opt. Commun. **391**, 68–76 (2017).
64. H. Yan, X. Li, B. Chandra, G. Tulevski, Y. Wu, M. Freitag, W. Zhu, P. Avouris, en F. Xia, "Tunable infrared plasmonic devices using graphene/insulator stacks," Nat. Nanotechnol. **7**(5), 330–334 (2012).
65. A. Farmani, M. Miri, en M. H. Sheikhi, "Design of a high extinction ratio tunable graphene on white graphene polarizer," IEEE Photonics Technol. Lett. **30**(2), 153–156 (2017).
66. C. Casiraghi, A. Hartschuh, E. Lidorikis, H. Qian, H. Harutyunyan, T. Gokus, K. S. Novoselov, en A. C. Ferrari, "Rayleigh imaging of graphene and graphene layers," Nano Lett. **7**(9), 2711–2717 (2007).
67. S. Johnson en J. Joannopoulos, "Block-iterative frequency-domain methods for Maxwell's equations in a planewave basis," Opt. Express **8**(3), 173 (2001).
68. S. D. Gedney, "Introduction to the Finite-Difference Time-Domain (FDTD) method for electromagnetics," Synth. Lect. Comput. Electromagn. **27**(1), 1–250 (2011).
69. H. Farmani, A. Farmani, en Z. Biglari, "A label-free graphene-based nanosensor using surface plasmon resonance for biomaterials detection," Phys. E Low-dimensional Syst. Nanostructures **116**, 113730 (2020).

Figures

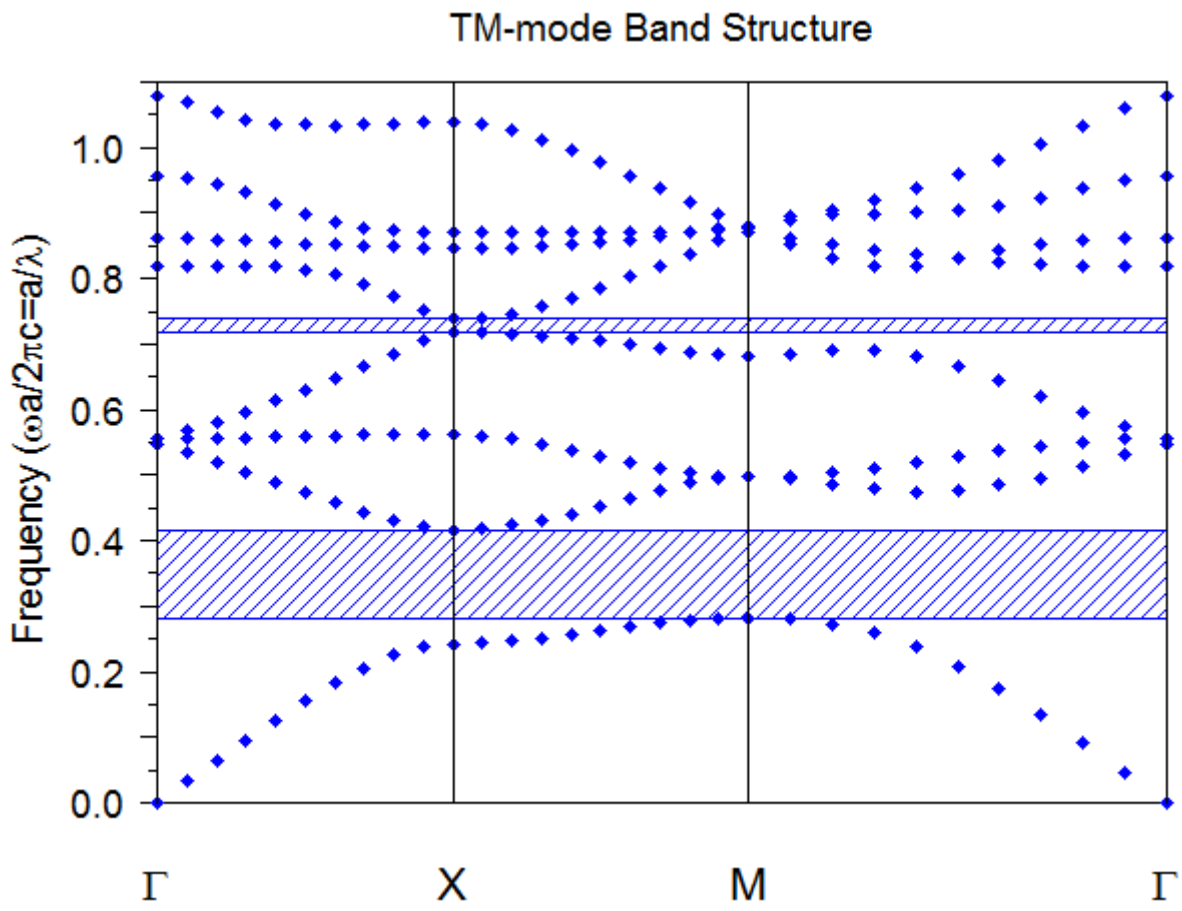

Figure 1

The band structure diagram of fundamental PhC in TM mode.

(a)

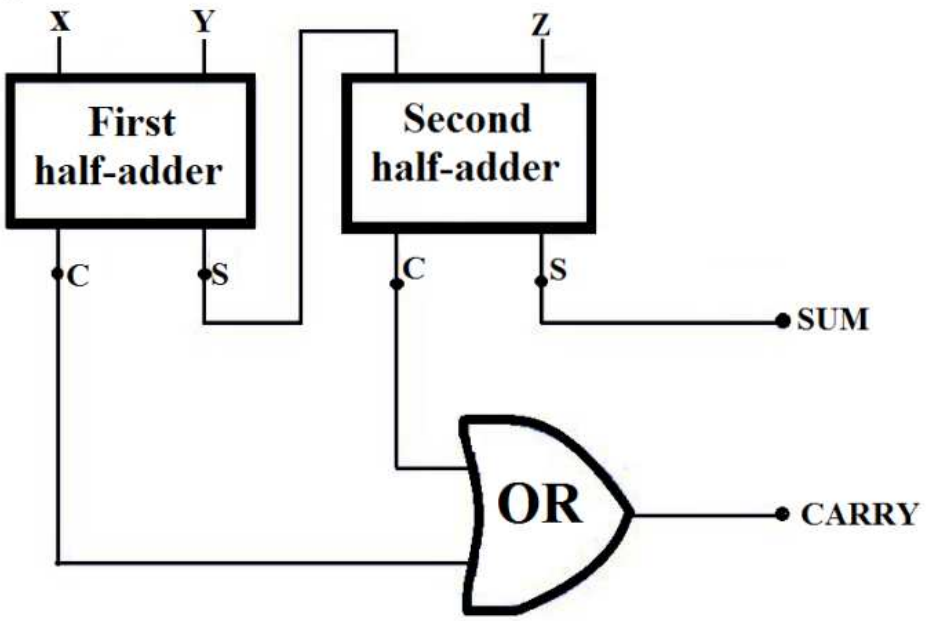

(b)

INPUT			OUTPUT	
X	Y	Z	SUM	CARRY
0	0	0	0	0
0	0	1	1	0
0	1	0	1	0
0	1	1	0	1
1	0	0	1	0
1	0	1	0	1
1	1	0	0	1
1	1	1	1	1

Figure 2

Illustration of (a) the typical full-adder circuit formed by two half-adders and an OR logic gate, three input ports of A, B, and Z, and two output ports of SUM and CARRY, (b) the truth table of full-adder for all states.

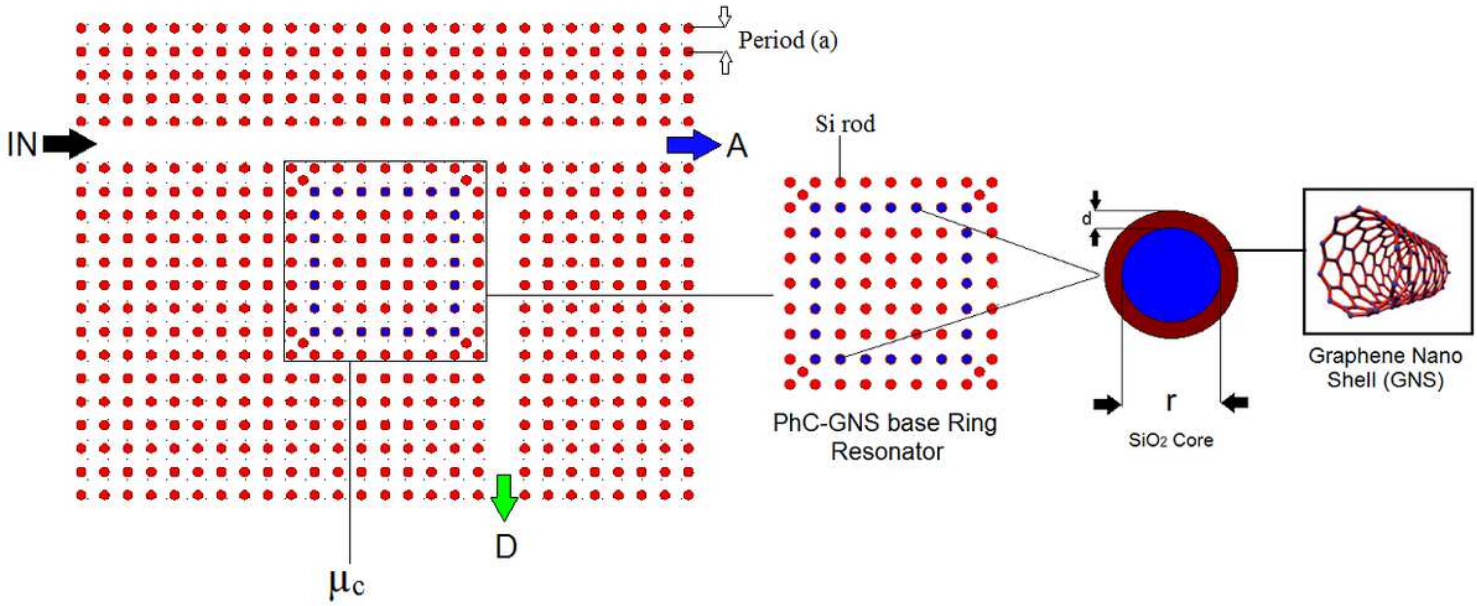

Figure 3

The schematic view of GNS-based PhC ring resonator and corresponding waveguides.

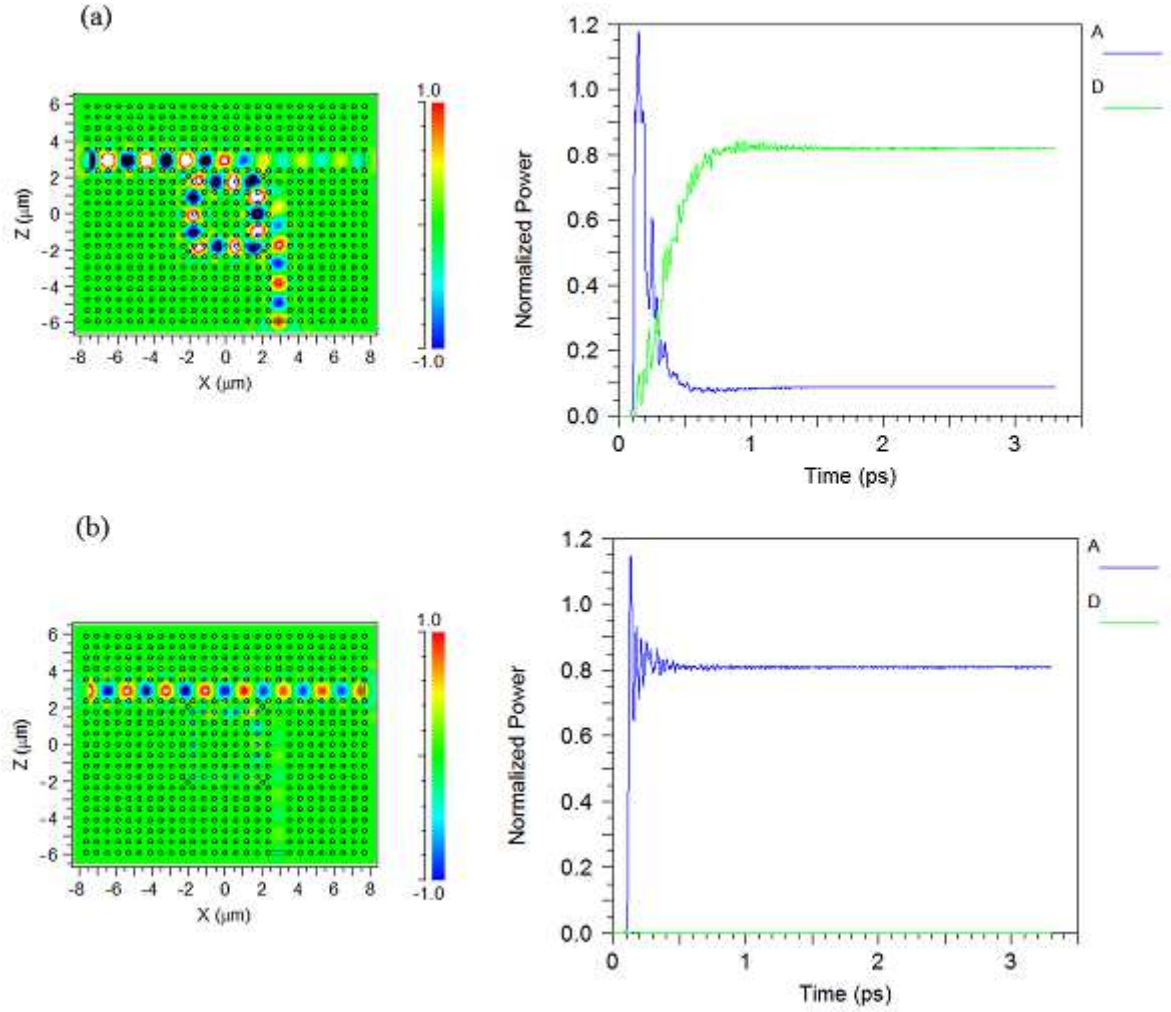

Figure 4

Light propagation inside the GNS base PhCRR for different values of μc (a) μc =0.5ev and (b) μc=0.3ev.

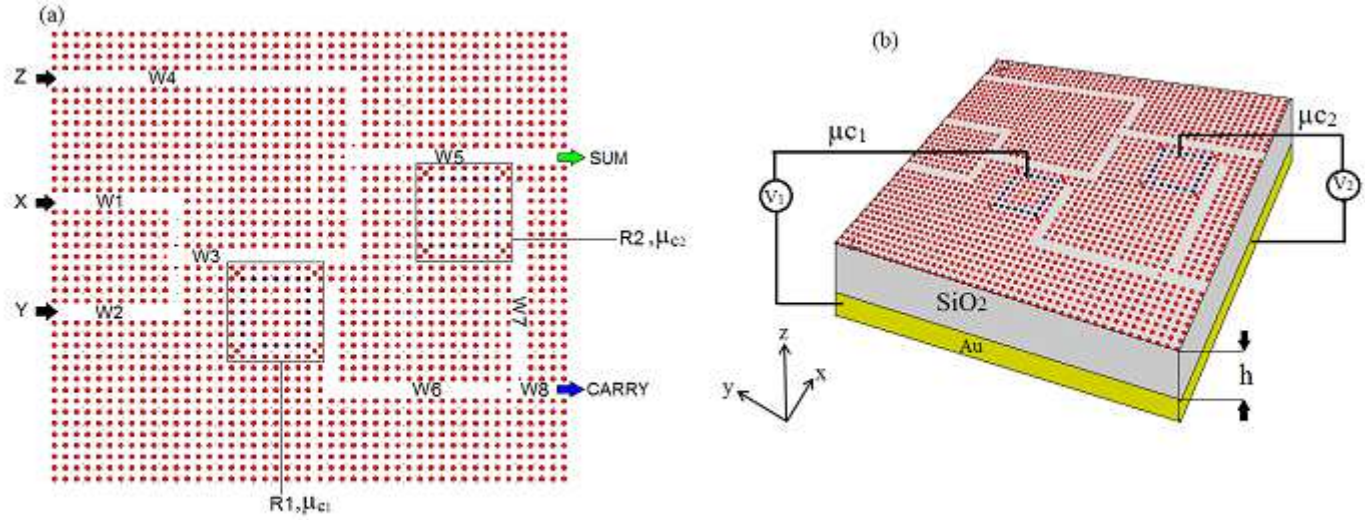

Figure 5

Illustration of the proposed full-adder, (a) top view of XY plane, and (b) the perspective view.

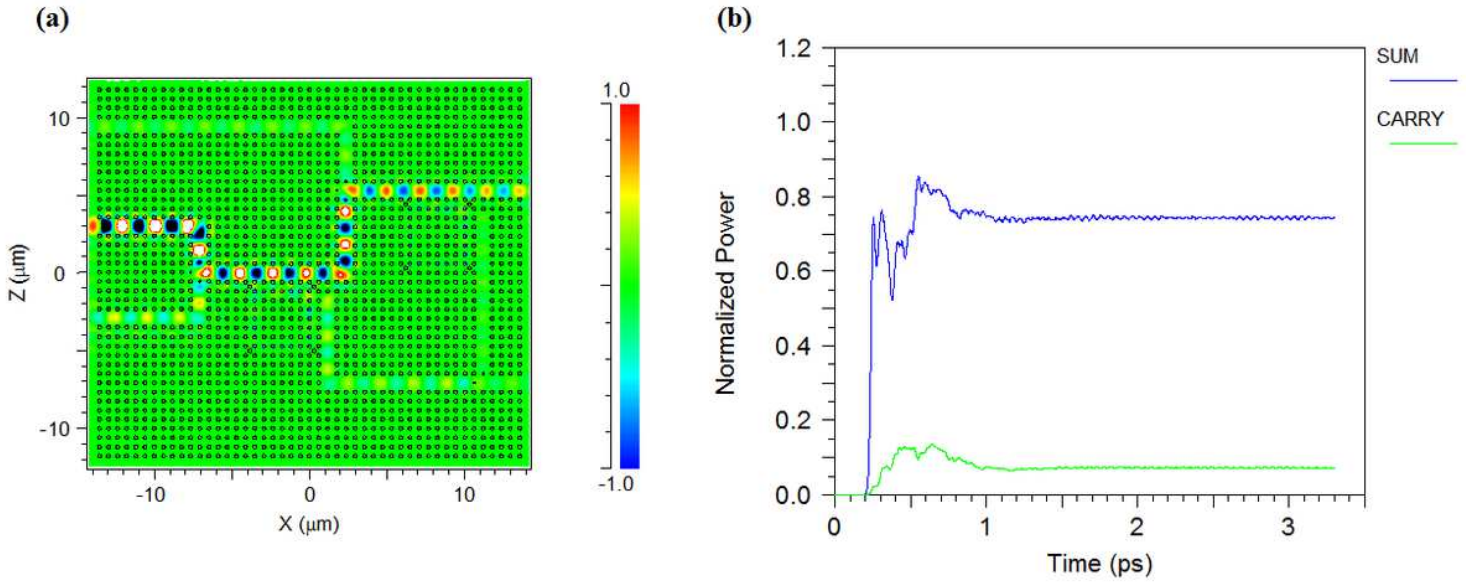

Figure 6

Illustration of (a) Light emission distribution and (b) normalized powers of the proposed optoelectronic full-adder using GNS-based PCRRs for Case #2.

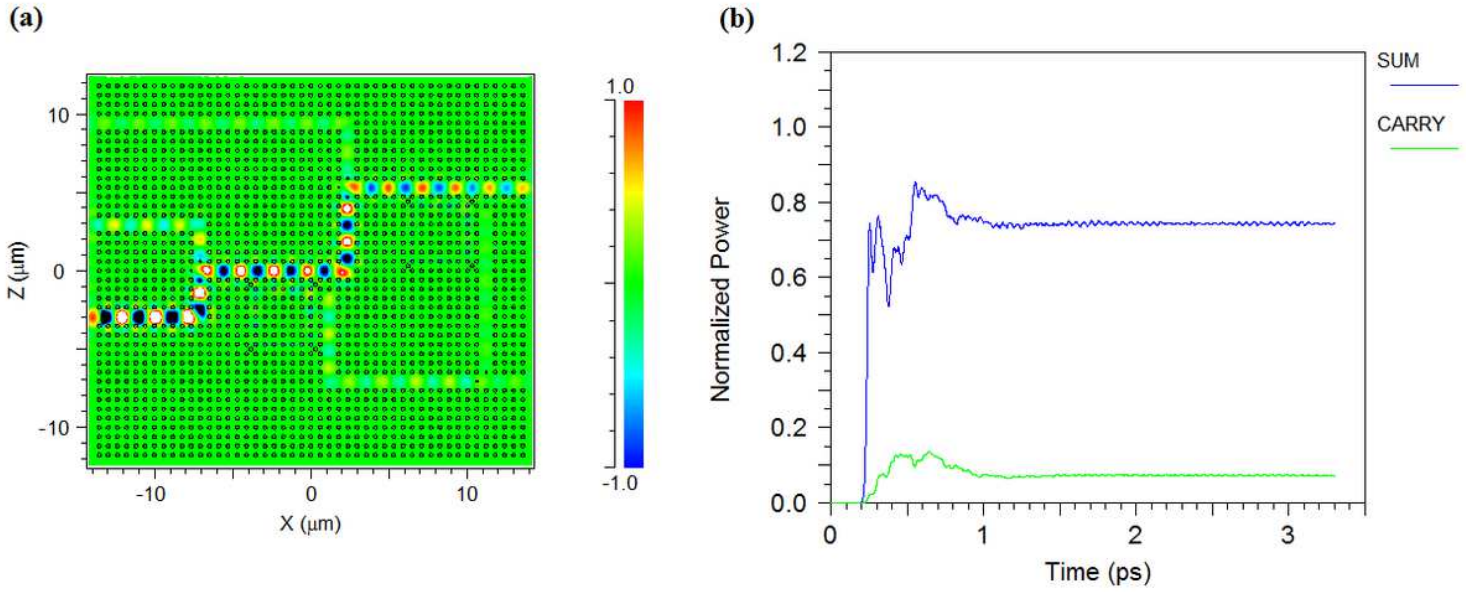

Figure 7

Illustration of (a) Light emission distribution and (b) normalized powers of the proposed optoelectronic full-adder using GNS-based PCRRs for Case #3.

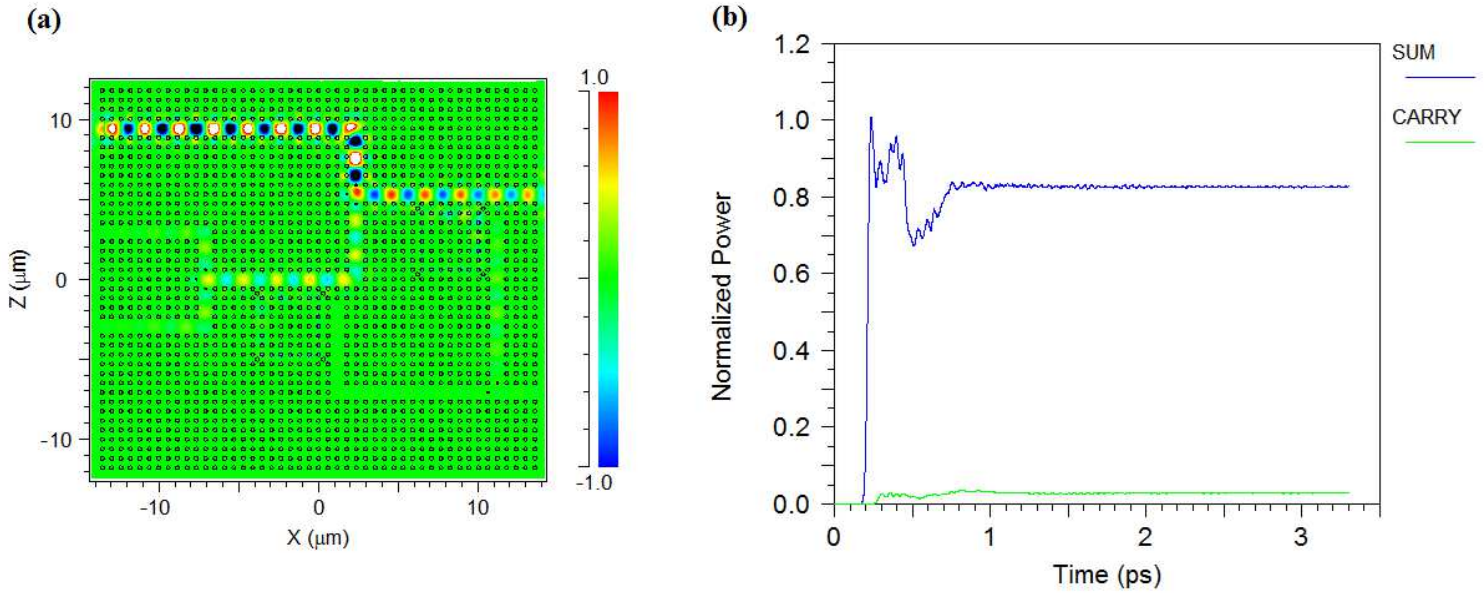

Figure 8

Illustration of (a) Light emission distribution and (b) normalized powers of the proposed optoelectronic full-adder using GNS-based PCRRs for Case #4.

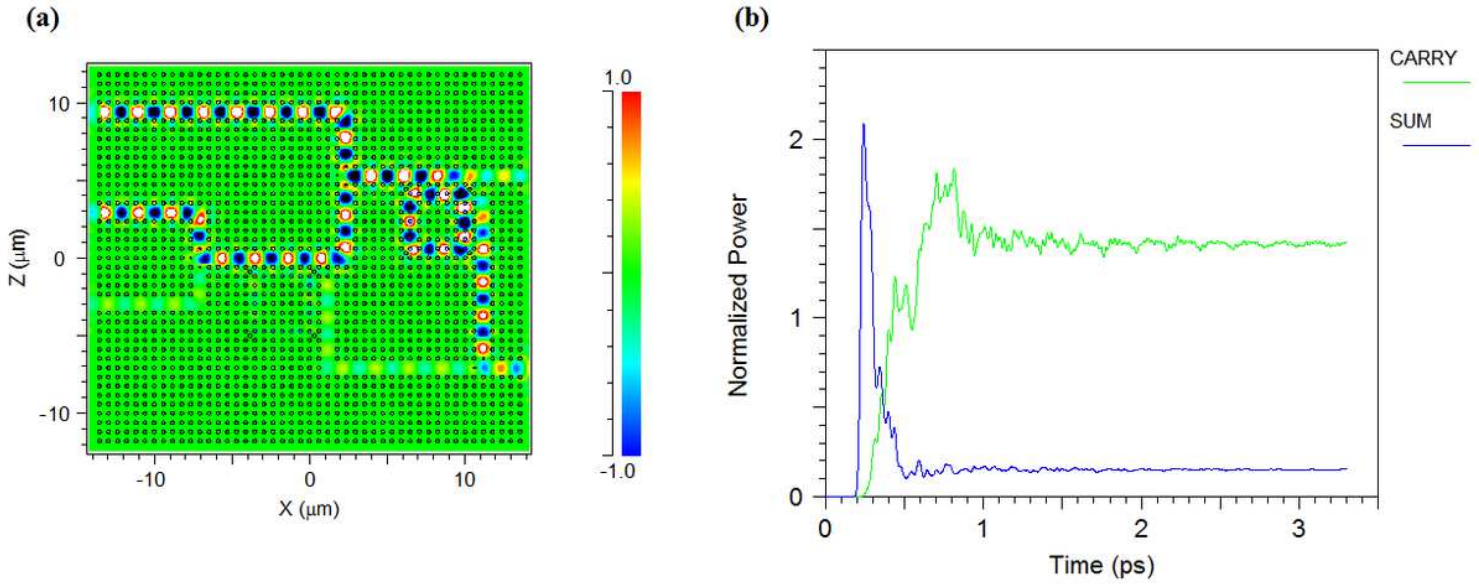

Figure 9

Illustration of (a) Light emission distribution and (b) normalized powers of the proposed optoelectronic full-adder using GNS-based PCRRs for Case #5.

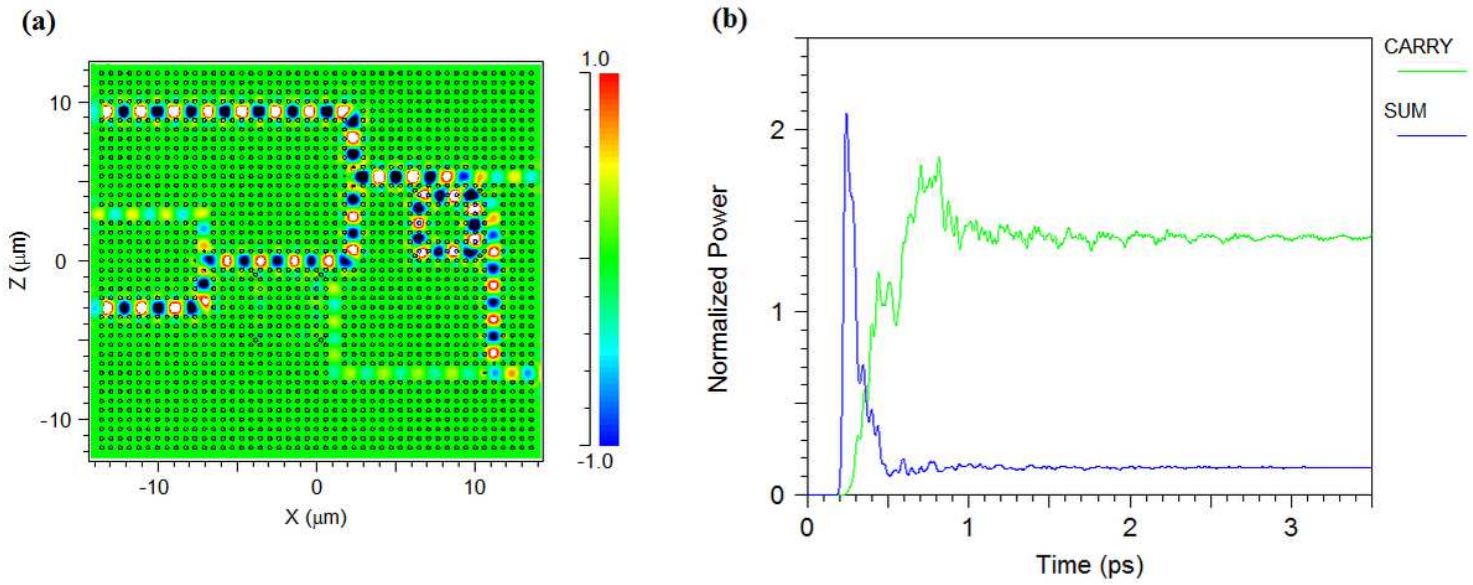

Figure 10

Illustration of (a) Light emission distribution and (b) normalized powers of the proposed optoelectronic full-adder using GNS-based PCRRs for Case #6.

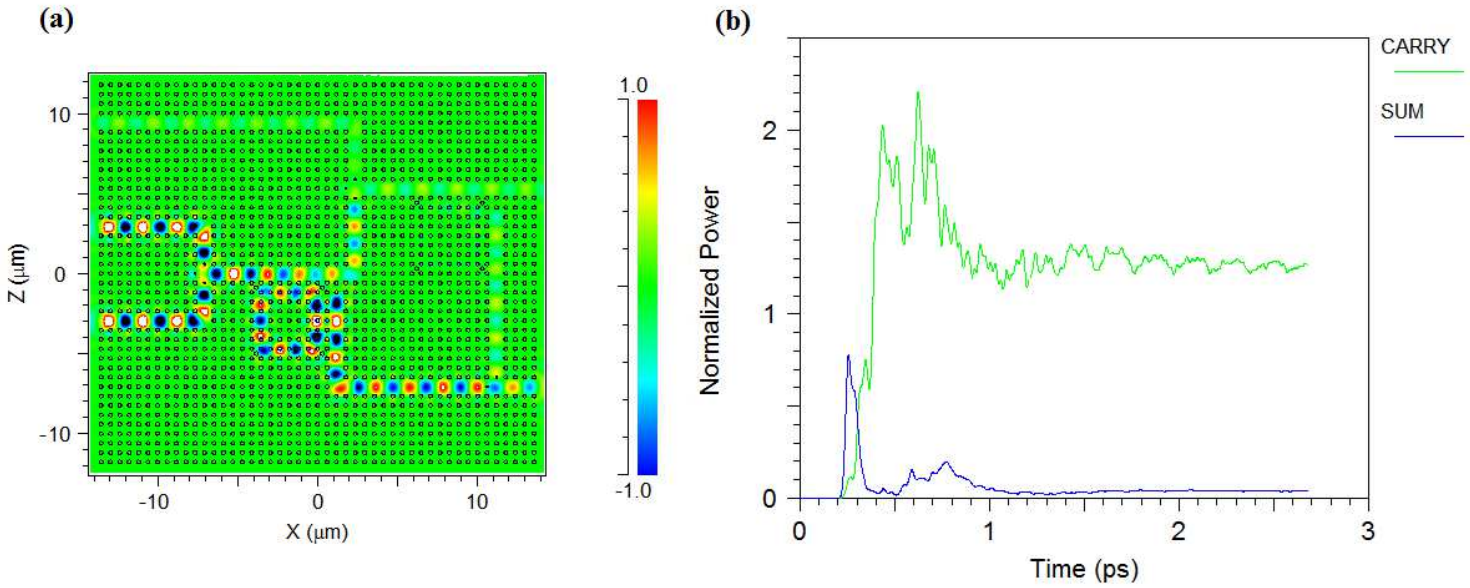

Figure 11

Illustration of (a) Light emission distribution and (b) normalized powers of the proposed optoelectronic full-adder using GNS-based PCRRs Case #7.

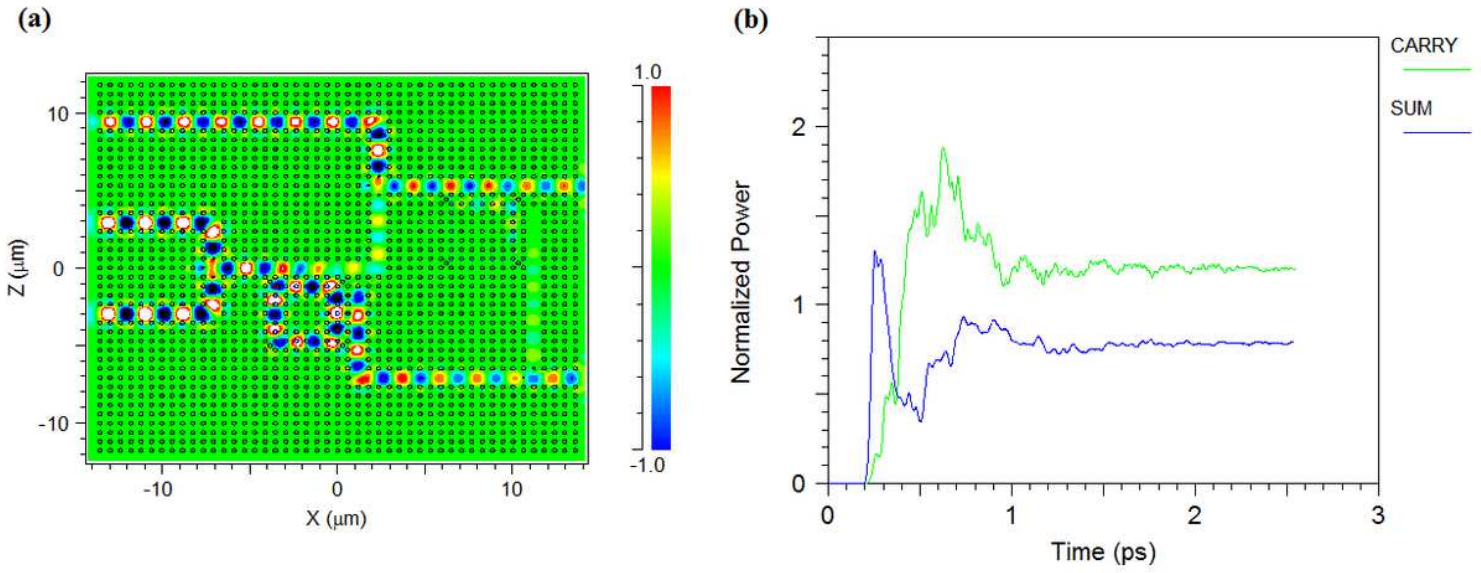

Figure 12

Illustration of (a) Light emission distribution and (b) normalized powers of the proposed optoelectronic full-adder using GNS-based PCRRs for Case #8.